Thin–Walled Structures 230 (2026) 115326

Contents lists available at ScienceDirect

Thin-Walled Structures

journal homepage: www.elsevier.com/locate/tws

Full length article

A semi-analytical model and synergistic mechanism for broadband sound radiation control in double-layer periodic acoustic black hole plates

Yuguang Chen [a], Debin Li [a], Fatao Ye [a], Li Cheng [b], Jie Deng [c], Liling Tang [a,*]

[a] School of Aeronautics and Astronautics, Shenzhen Campus, Sun Yat-Sen University, Shenzhen, China
[b] Department of Mechanical Engineering, The Hong Kong Polytechnic University, Hung Hom, Kowloon, Hong Kong, China
[c] Human-Environment Research (HER) group, Department of Engineering, La Salle, Universitat Ramon Llull C/Quatre Camins 30, Barcelona, Catalonia 08022, Spain

ARTICLE INFO

Keywords:
Acoustic black hole
Structural intensity
Periodic plates
Asymmetric sound radiation
Synergistic mechanism

ABSTRACT

Low-frequency vibration and noise control of lightweight structures remains a critical engineering challenge. While acoustic black hole (ABH) structures offer a promising lightweight passive solution, existing designs suffer from venerable structural stiffness and low-frequency deficiency. To address these issues, this study investigates a composite double-layer periodic ABH plate that integrates lightweight property, broadband performance, and high stiffness compared with conventional single-layer ABH plates. Through combining the Gaussian expansion method (GEM) and radiation impedance matrix, the vibroacoustic response of the system can be efficiently and accurately predicted by a semi-analytical sound radiation model, as demonstrated through comparisons with Finite Element simulations. Both numerical and experimental results confirm the structure's superior broadband sound suppression ability when compared with a uniform plate of equivalent mass, evidenced by a substantial reduction in radiated sound power within its flexural wave bandgap, and extension to frequencies far below the cut-on frequency of a single ABH unit with damping treatment. Analyses reveal the asymmetric vibration and sound radiation between the two plate facets when excitation is applied to the ABH region, a phenomenon stemming from the synergetic effects of the ABH, bandgaps and the double-layer design: within bandgaps, energy localization combined with ABH-induced wave retarding impairs the radiation efficiency of the excited plate; outside bandgaps, the ABH effect and double-layer configuration facilitates a sequential energy concentration-dissipation process, leading to strong suppression of the output plate's vibration and sound radiation. This work elucidates the underlying mechanisms of the composite periodic ABH structures, and provides an efficient analytical tool for designing lightweight, low-noise engineering structures.

1. Introduction

The control of low-frequency vibration and noise in lightweight structures remains a critical challenge in aerospace, high-speed transportation, and many other fields. Conventional designs are constrained by the mass law governing the sound transmission of panels, which hinders the simultaneous achievement of lightweight construction and superior sound insulation performance. The acoustic black hole (ABH) effect provides a promising solution to address this dilemma by realizing a power-law gradient design of structural thickness or material parameters [1–3]. The outcome is to reduce the phase/group velocities of flexural waves, thereby concentrating vibration energy within the ABH region, where it can be efficiently dissipated with minimal damping. Therefore, ABH structures are regarded as a promising lightweight passive solution for vibration and noise mitigation, as substantiated by numerous theoretical [4–6] and experimental [7–9] studies.

ABH structures also demonstrate considerable potential in sound radiation control [10]. Prior research has employed methods such as coupled finite element-boundary element [11], transfer matrix [12], Rayleigh-Ritz wavelet expansion [13] to investigate the sound radiation characteristics and suppression mechanisms of various ABH structures (such as plates, beams, and cavity-coupled systems [14]). These studies confirm the superior mid-to-high frequency sound radiation efficacy of various ABH designs. Moreover, add-on ABH-based dynamic vibration absorbers have also been proven to entail broadband sound radiation suppression effect through vibration reduction of the radiating structures [15,16]. However, most existing research focuses on basic ABH configurations, such as beams or plates with simple embedded single or

* Corresponding author.
E-mail address: tanglling@sysu.edu.cn (L. Tang).

https://doi.org/10.1016/j.tws.2026.115326
Received 6 February 2026; Received in revised form 18 May 2026; Accepted 25 June 2026
Available online 27 June 2026

multiple ABH indentations. These designs suffer from two inherent limitations: first, the substantial thickness reduction in the ABH region adversely compromises the overall structural stiffness [17]; second, systematic ABH effects typically play out above the cut-on frequency [18], which again severely restricts the applicability to low-frequency range, which remains a bottle-necking challenge, critical to many engineering applications.

To address these low-frequency limitations, researchers have explored combining ABH with periodic structures. Bandgaps generated through Bragg scattering or local resonance effects can effectively suppress elastic wave propagation within specific frequency ranges, offering a viable approach for designing broadband, efficient vibration and noise control systems [19–22]. Periodic structures based on simple embedded ABH units have shown proven effectiveness in reducing vibration and sound radiation [23–39]. However, these designs still suffer from the compromised structural strength due to the thickness thinning. While add-on ABH units as additional structures [40–44] can alleviate this issue, they simultaneously introduce extra mass and increase structural bulkiness. To overcome these drawbacks, our previous work proposed a composite double-layer periodic ABH structures [45–48]. These configurations not only achieve sub-wavelength broadband flexural wave bandgap but also maintain lightweight properties and relatively high structural strength, holding promise for low-frequency broadband vibration and noise control. However, the layered vibration behavior observed in more complex multi-layer designs [49] may give rise to intricate acoustic radiation phenomena. The interplay among the layered configuration, ABH effects, and bandgap characteristics remains insufficiently understood. Furthermore, due to the complexity of such composite structures and their associated sound radiation behavior, existing studies rely on computationally intensive finite element simulations or experimental tests. In this regard, more computationally efficient and versatile simulation models are needed for analyzing and optimizing engineering designs.

To bridge this research gap, this study establishes a semi-analytical acoustic radiation model based on Gaussian expansion method (GEM) [50] for composite double-layer periodic ABH plates. While the GEM has been previously applied to single-layer ABH plates [51], its application to double-layer periodic ABH plates with coupled layers and sound radiation analysis has not been reported. This work presents the first semi-analytical framework that extends GEM to vibroacoustic analysis of such composite double-layer periodic ABH structures, enabling efficient and accurate predictions of sound radiation performance that would otherwise require computationally expensive finite element simulations.

The remainder of this paper is organized as follows. Section 2 establishes the semi-analytical acoustic radiation model for the composite ABH structure and describes the wavenumber spectrum and structural intensity methods used for mechanistic analysis. Section 3 validates the model's accuracy and verifies its computational efficiency via finite element simulations. The sound radiation performance of the ABH plate with that of a uniform plate is then compared and scrutinized. Wavenumber and structural intensity analyses are conducted to elucidate the sound radiation mechanisms and the physical origin of the observed sound radiation differences. Section 4 presents experimental validation in terms of sound radiation. Finally, Section 5 summarizes the main conclusions.

2. Theoretical model and analysis method

2.1. Problem description

As shown in Fig. 1(a), we consider a plate composed of a 5×5 periodically arranged ABH unit cells. The geometry of a unit cell is depicted in Fig. 1(b), where a and H denote the lattice constant and the total cell thickness, respectively. Each unit cell comprises two plate/facets, each featuring symmetrical ABH indentations on the upper and lower surfaces. These two plates are coupled via distributed virtual springs with high stiffness aligned along the x, y, and z directions, as illustrated in Fig. 1(c). The thickness of the ABH profile is tailored according to $h(x) = \varepsilon x^m + h_0$ with m being the taper power index, h_0 the residual truncation thickness, as shown in a cross-sectional view in Fig. 1 (d). The radial length of the ABH isl_{ABH}. To ensure structural integrity and effective bandgap formation, the condition $\sqrt{2}l_{\mathrm{ABH}} < a < 2l_{\mathrm{ABH}}$ is satisfied [49]. Without loss of generality, a point force $f(t)$ is applied at a location$(x_f y_f)$, as shown in Fig. 1(a), which can be positioned either in the uniform region or within the ABH region. For clarity, the plate facet directly subjected to the external excitation is referred to as input plate (Plate 1), while the opposing plate output plate (Plate 2).

2.2. Vibration response of the composite ABH plate

We employ the GEM [50] to formulate the kinetic and potential energies of Plate 1 and Plate 2, respectively. The system Lagrangian is then constructed by incorporating the coupling energy from the virtual

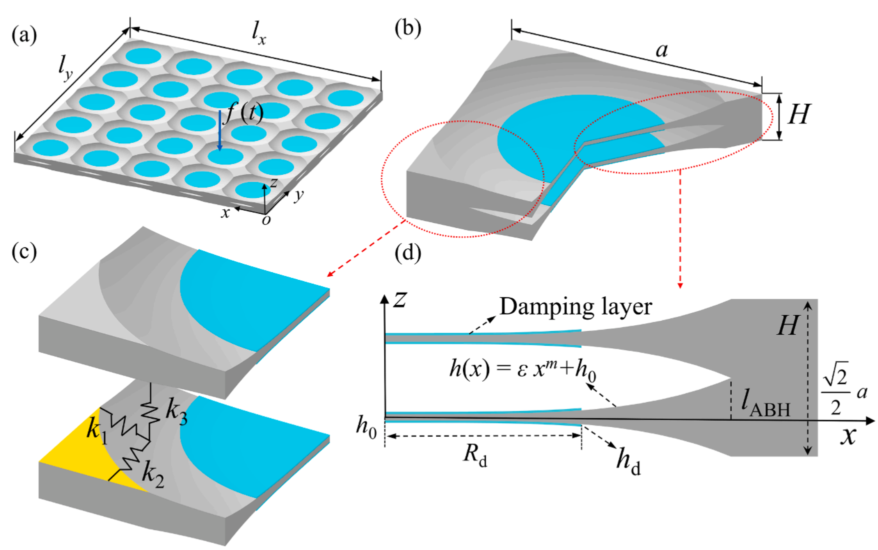

Fig. 1. Structure model: (a) a plate composed of 5×5 unit cells under a harmonic point force excitation; (b) a single unit cell and its sectional view; (c) coupling through distributed virtual springs k_1, k_2, and k_3 along x, y, and z directions; (d) local cross section view corresponding to the area enclosed by the red dash line in (b).

springs. By solving the Lagrange equations, the vibration response of the composite ABH plate structure is derived. Specifically, the in-plane displacements u, v, and the out-of-plane displacement w for each plate (i=1,2) are expanded in terms of shape functions as follows:

$$\begin{aligned} u_i(x,y,t) &= \mathbf{a}_i^T(t)\boldsymbol{\chi}(x,y) \\ v_i(x,y,t) &= \mathbf{b}_i^T(t)\boldsymbol{\gamma}(x,y) \\ w_i(x,y,t) &= \mathbf{c}_i^T(t)\boldsymbol{\zeta}(x,y) \end{aligned} \tag{1}$$

The displacement shape functions for each direction can be constructed as the Kronecker product of one-dimensional Gaussian basis functions :

$$\begin{aligned} \boldsymbol{\chi}(x,y) &= \boldsymbol{\alpha}^{\chi}(x)\otimes\boldsymbol{\beta}^{\chi}(y) \\ \boldsymbol{\gamma}(x,y) &= \boldsymbol{\alpha}^{\gamma}(x)\otimes\boldsymbol{\beta}^{\gamma}(y) \\ \boldsymbol{\zeta}(x,y) &= \boldsymbol{\alpha}^{\zeta}(x)\otimes\boldsymbol{\beta}^{\zeta}(y) \end{aligned} \tag{2}$$

where $\otimes$ denotes the Kronecker product; $\boldsymbol{\alpha}$ or $\boldsymbol{\beta}$ is a column vector containing Gaussian basis functions dependent solely on the x or y direction, i.e.,

$$\begin{aligned} \boldsymbol{\alpha}(x) &= [\alpha_1,\alpha_2,\ldots,\alpha_m]^{\mathrm{T}} \\ \boldsymbol{\beta}(x) &= [\beta_1,\beta_2,\ldots,\beta_n]^{\mathrm{T}} \end{aligned} \tag{3}$$

with

$$\alpha_{X_i}^{g}(x) = 2^{\frac{g}{2}}\exp\left[-\frac{(2^g x - X_i)^2}{2}\right],\beta_{Y_i}^{p}(y) = 2^{\frac{p}{2}}\exp\left[-\frac{(2^p y - Y_i)^2}{2}\right] \tag{4}$$

Here g and p are scaling parameters that control the stretching or compression of the basis functions, and X and Y are translation parameters that move the functions. For the general case of a rectangular plate comprising $[x_{\mathrm{L}},x_{\mathrm{R}}]\times[y_{\mathrm{L}},y_{\mathrm{R}}]$, the parameters can be selected using the expressions :

$$\begin{aligned} &g \geq \mathrm{ceil}\left(\log_2\frac{6}{x_{\mathrm{R}}-x_{\mathrm{L}}}\right), X = [-3+\mathrm{floor}(2^g x_{\mathrm{L}}), 3+\mathrm{ceil}(2^g x_{\mathrm{R}})] \\ &p \geq \mathrm{ceil}\left(\log_2\frac{6}{y_{\mathrm{R}}-y_{\mathrm{L}}}\right),\ Y = [-3+\mathrm{floor}(2^p y_{\mathrm{L}}), 3+\mathrm{ceil}(2^p y_{\mathrm{R}})] \end{aligned} \tag{5}$$

where ceil(*) returns the smallest integer greater than or equal to *, floor (*) returns the largest integer less than or equal to *.

Based on classical Kirchhoff-Love thin plate theory, the kinetic energy and potential energies of each ABH plate (i=1, 2) write:

$$E_{\mathrm{K}}^{i} = \frac{1}{2}\int_0^{l_x}\int_0^{l_y}\rho_i h_i(x,y)\left(\dot{u}_i^2+\dot{v}_i^2+\dot{w}_i^2\right)\mathrm{d}x\mathrm{d}y = \frac{1}{2}\dot{\mathbf{d}}_i^{\mathrm{T}}\mathbf{M}_i\dot{\mathbf{d}}_i \tag{6}$$

$$\begin{aligned} E_{\mathrm{P}}^{i} =& \frac{1}{2}\int_0^{l_x}\int_0^{l_y} D_i\begin{bmatrix}\left(\frac{\partial^2 w_i}{\partial x^2}\right)^2+\left(\frac{\partial^2 w_i}{\partial y^2}\right)^2+\upsilon_i\left(\frac{\partial^2 w_i}{\partial x^2}\frac{\partial^2 w_i}{\partial y^2}+\frac{\partial^2 w_i}{\partial y^2}\frac{\partial^2 w_i}{\partial x^2}\right)\\ +2(1-\upsilon_i)\left(\frac{\partial^2 w_i}{\partial x\partial y}\right)^2\end{bmatrix}\mathrm{d}x\mathrm{d}y \\ &+\frac{1}{2}\int_0^{l_x}\int_0^{l_y} D_{\mathrm{E}}^{i}\begin{bmatrix}\left(\frac{\partial u_i}{\partial x}\right)^2+\left(\frac{\partial v_i}{\partial y}\right)^2+\upsilon_i\left(\frac{\partial u_i}{\partial x}\frac{\partial v_i}{\partial y}+\frac{\partial v_i}{\partial y}\frac{\partial u_i}{\partial x}\right)\\ +\frac{1-\upsilon_i}{2}\left(\frac{\partial u_i}{\partial x}+\frac{\partial v_i}{\partial y}\right)^2\end{bmatrix}\mathrm{d}x\mathrm{d}y \\ &= \frac{1}{2}\mathbf{d}_i^{\mathrm{T}}\mathbf{K}_i\mathbf{d}_i \end{aligned} \tag{7}$$

where $\mathbf{d}_i = [\mathbf{a}_i^T\mathbf{b}_i^T\mathbf{c}_i^T]^{\mathrm{T}}$, $h_i(x,y)$ denotes the spatially varying thickness of the plate i, ρ_i denotes the material density, υ_i stands for the Poisson ratio, $D_i = E_i^{*}h_i(x,y)^3/12(1-\upsilon_i^2)$ is the local flexural stiffness, $D_{\mathrm{E}}^{i} = E_i^{*}h_i(x,y)/(1-\upsilon_i^2)$ indicates the local tension-compression stiffness, $E_i^{*} = E_i(1+\mathrm{j}\eta_i)$ is the complex Young's modulus and η_i is the material loss factor.

The viscoelastic layer is treated as fully-coupled to the bare plate with its kinetic and potential energy contributing to the whole system [5], which can be expressed as:

$$E_{\mathrm{K,d}}^{i} = \frac{1}{2}\dot{\mathbf{d}}_i^{\mathrm{T}}\mathbf{M}_{i,\mathrm{d}}\dot{\mathbf{d}}_i, E_{\mathrm{P,d}}^{i} == \frac{1}{2}\mathbf{d}_i^{\mathrm{T}}\mathbf{K}_{i,\mathrm{d}}\mathbf{d}_i \tag{8}$$

The work done by external forces can be expressed as:

$$\begin{aligned} W =& \int_0^{l_x}\int_0^{l_y} f(t)w_i\left(x_f,y_f,t\right)\mathrm{d}x\mathrm{d}y = \mathbf{d}_i^{\mathrm{T}}\left[f(t)\int_0^{l_x}\int_0^{l_y}\zeta\left(x_f,y_f\right)\mathrm{d}x\mathrm{d}y\right] \\ &\equiv \mathbf{d}_i^{\mathrm{T}}\mathbf{f}(t) \end{aligned} \tag{9}$$

The coupling between the two plates via three sets of distributed virtual springs (see Fig. 1(c)) is described by the following conditions:

$$\begin{aligned} &\lim_{k_1\to\infty}\left[\left(u_1+\frac{h_{\mathrm{uni},1}}{2}\frac{\partial w_1}{\partial x}\right)-\left(u_2-\frac{h_{\mathrm{uni},2}}{2}\frac{\partial w_2}{\partial x}\right)\right]=0 \\ &\lim_{k_2\to\infty}\left[\left(v_1+\frac{h_{\mathrm{uni},1}}{2}\frac{\partial w_1}{\partial y}\right)-\left(v_2-\frac{h_{\mathrm{uni},2}}{2}\frac{\partial w_2}{\partial y}\right)\right]=0 \\ &\lim_{k_3\to\infty}(w_1-w_2)=0 \end{aligned} \tag{10}$$

with $h_{\mathrm{uni},i}$ being the thickness of the uniform region of plate i. This sign convention follows the kinematic relations of thin plate theory: for positive flexural rotation, a point on the lower surface moves in the positive x-direction, while a point on the upper surface moves in the negative x-direction. Therefore, the corresponding coupling potential energy derived from Equation (10) can be written as:

$$\begin{aligned} E_{\mathrm{coup}} =& \frac{1}{2}k_1\int_{A_{\mathrm{c}}}\left(u_1+\frac{h_{\mathrm{uni},1}}{2}\frac{\partial w_1}{\partial x}-u_2+\frac{h_{\mathrm{uni},2}}{2}\frac{\partial w_2}{\partial x}\right)^2 dA_{\mathrm{c}} \\ &+\frac{1}{2}k_2\int_{A_{\mathrm{c}}}\left(v_1+\frac{h_{\mathrm{uni},1}}{2}\frac{\partial w_1}{\partial y}-v_2+\frac{h_{\mathrm{uni},2}}{2}\frac{\partial w_2}{\partial y}\right)^2 dA_{\mathrm{c}} \\ &+\frac{1}{2}k_3\int_{A_{\mathrm{c}}}(w_1-w_2)^2 dA_{\mathrm{c}} = \frac{1}{2}\mathbf{q}^{\mathrm{T}}\mathbf{K}_{\mathrm{coup}}\mathbf{q} \end{aligned} \tag{11}$$

where $\mathbf{q} = \left[\mathbf{d}_1^T \quad \mathbf{d}_2^T\right]^T$, A_{c} denotes the connection area between the two plates. From Equations (6), (7), (8) and (11), we can assemble the global mass matrix and stiffness matrix of the coupled system:

$$\mathbf{M} = \begin{bmatrix}\mathbf{M}_1+\mathbf{M}_{1,\mathrm{d}} & \\ & \mathbf{M}_2+\mathbf{M}_{2,\mathrm{d}}\end{bmatrix} \quad \mathbf{K} = \begin{bmatrix}\mathbf{K}_1+\mathbf{K}_{1,\mathrm{d}} & \\ & \mathbf{K}_2+\mathbf{K}_{2,\mathrm{d}}\end{bmatrix}+\mathbf{K}_{\mathrm{coup}} \tag{12}$$

The Lagrangian of the system writes:

$$L = E_{\mathrm{K}}-E_{\mathrm{P}}+W = \frac{1}{2}\dot{\mathbf{q}}^{\mathrm{T}}\mathbf{M}\dot{\mathbf{q}}-\frac{1}{2}\mathbf{q}^{\mathrm{T}}\mathbf{K}\mathbf{q}+\mathbf{q}^{\mathrm{T}}\mathbf{f}(t) \tag{13}$$

Applying the Euler–Lagrange equation $\frac{d}{dt}\left(\frac{\partial L}{\partial\dot{\mathbf{q}}(t)}\right)-\frac{\partial L}{\partial\mathbf{q}(t)}=0$ yields the vibration equation :

$$\mathbf{M}\ddot{\mathbf{q}}(t)+\mathbf{K}\mathbf{q}(t) = \mathbf{f}(t) \tag{14}$$

Assuming a harmonic excitation and motion, i.e., $\mathbf{f}(t) = \widehat{\mathbf{F}}e^{j\omega t}$ and $\mathbf{q}(t) = \widehat{\mathbf{q}}e^{j\omega t}$, the steady-state vibration response can be obtained by solving:

$$\left[\mathbf{K}-\omega^2\mathbf{M}\right]\widehat{\mathbf{q}} = \widehat{\mathbf{F}} \tag{15}$$

2.3. Acoustic radiation model

The plate is assumed to be mounted on an infinite rigid baffle to eliminate sound wave diffraction at the edges. Based on elementary radiator approach, the plate surface is discretized into sufficiently small rectangular elements through a finite element mesh. Using the normal velocity vector $\boldsymbol{v}$ of each surface element obtained from the vibration analysis (Section 2.2), the sound pressure vector can be expressed by using the radiation impedance matrix $\boldsymbol{Z}$ as:

$$\mathbf{p} = \mathbf{Z}\mathbf{v} \tag{16}$$

where $Z_{ij} = \mathrm{j}\omega\rho_0 S_e e^{-\mathrm{j}kR_{ij}}/2\pi R_{ij}$ with ρ_0 being the density of air, ω and k the angular frequency and wavenumber, respectively, S_e the element area, andR_{ij} the distance between the ith and jth elements.

Then, the total sound power radiated by the plate can be obtained by summing the contributions from all elements:

$$W = \sum_{i=1}^{N} \frac{1}{2} S_\mathrm{e} \mathrm{Re}\{v_i^* p_i\} = \frac{S_\mathrm{e}}{2} \mathrm{Re}\{\mathbf{v}^H \mathbf{Z}\mathbf{v}\} \tag{17}$$

in which * and H represent complex conjugate and Hermitian transpose, respectively; N is the total number of surface elements.

The sound radiation efficiency is defined as :

$$\sigma = \frac{W}{\rho_0 c_0 S \langle \overline{v^2} \rangle} \tag{18}$$

where c_0 is the sound speed;$\langle \overline{v^2} \rangle$ is the mean quadratic velocity (MQV) over the whole vibration surface, which can be expressed as$\langle \overline{v^2} \rangle = (S_e/2S)\boldsymbol{v}^H\boldsymbol{v}$ with S being the total plate surface area.

2.4. Analysis method

The wavenumber spectra decompose the vibration field into its constituent wavenumber components. The amplitude distribution within the wavenumber spectrum informs the energy distribution associated with supersonic (radiating) and subsonic (non-radiating) waves, providing direct insights into the sound radiation mechanism of the composite ABH plate structure.

Specifically, the velocity field $v(x, y, f)$ in the spatial domain can be transformed into the wavenumber domain through a two-dimensional Fourier transform :

$$V\left(k_x, k_y, f\right) = \iint v(x, y, f) e^{-\mathrm{j}k_x x} e^{-\mathrm{j}k_y y} dxdy \tag{19}$$

For a given frequency f, a radiation circle is defined in the wavenumber domain with a radius equal to the acoustic wavenumber $k_c = \omega/c_0$. Structural wavenumber components with $\sqrt{k_x^2 + k_y^2} < k_c$ (inside the circle) are supersonic and contribute efficiently to far field sound radiation. Components outside this circle are subsonic and evanescent, contributing negligibly to far-field sound radiation [52]. Therefore, by analyzing the energy distribution of the wavenumber spectrum inside and outside the radiation circle, the sound radiation behavior of the ABH structure can be characterized.

On the other hand, the composite double-layer ABH structure exhibits distinct layered vibration characteristics. Structural intensity analysis, which calculates vibration energy flow from the product of vibratory velocities and internal forces, is expected to reveal the energy transmission paths, energy-sink distributions, and dissipation characteristics within such structures [53–55]. This helps elucidate how the ABH effect, bandgap characteristics and layered configuration interact with each other to influence the overall sound radiation behavior.

Structural intensity is defined as the vibrational power flow per unit cross-sectional area. Its vector form reflects both the magnitude and direction of the energy flow. For a thin plate, it can be expressed as [56] :

$$\begin{aligned} I_x &= -\frac{1}{2}\mathrm{Re}\left(N_x \dot{u}^* + N_{xy}\dot{v}^* + Q_x \dot{w}^* + M_x \dot{\theta}_y^* - M_{xy}\dot{\theta}_x^*\right) \\ I_y &= -\frac{1}{2}\mathrm{Re}\left(N_y \dot{u}^* + N_{yx}\dot{v}^* + Q_y \dot{w}^* - M_y \dot{\theta}_x^* + M_{yx}\dot{\theta}_y^*\right) \end{aligned} \tag{20}$$

where N_x, N_y, and $N_{xy} = N_{yx}$ are complex membrane and in-plane shear forces, Q_x, Q_y are complex transverse shear forces, M_x, M_y are complex flexural moments, $M_{xy} = M_{yx}$ are complex twisting moments, and θ_x, θ_y are angular displacements. Detailed formulas are provided in Appendix A.

3. Numerical results and discussions

3.1. Model validation

The proposed sound radiation model is first validated against FEM simulations. The geometrical and material parameters for the input and output plates are identical, as detailed in Table 1. When damping layers are applied, the radius of 47.25 mm covers approximately 75% of the ABH radial length ($l_\mathrm{ABH} = 63$ mm) to ensure both effective energy dissipation and limited mass increase. A parametric study on the influence of the damping coverage ratio is provided in Appendix B. In the present model, we take $g = p = 6.5$, so that $X = Y = [-3, 49]$ and thus each displacement shape function have dimensions of 2809×1. For comparison, the FEM model is established in the 3D Solid Mechanics module of COMSOL Multiphysics. To ensure computational accuracy, each wavelength must include at least 6 mesh elements, which results in total 367,904 tetrahedral elements and 4963,434 ° of freedom (DOFs). Considering the special structural design, ABH region constitutes approximately 95% of the entire structure, implying that external forces are therefore more likely to act on the ABH region rather than on the uniform substrate in practical applications. To examine the sound radiation characteristics under a typical loading condition, a unit harmonic excitation force is applied to the ABH region at (17.5 mm , 17.5 mm). The boundaries of the structure are set as all free.

Fig. 2 compares the radiated sound power of the output plate obtained from the present theoretical model and FEM simulation, both with and without damping layers. Good agreement is observed across the entire frequency range, confirming the accuracy of the proposed acoustic radiation model. The increasing error at higher frequencies is likely due to the neglected shear effect in the theoretical model. Notably, the theoretical model exhibits remarkable computational efficiency. Under the same computing platform (Intel® Xeon® Gold 6248 R , 3.00 GHz CPU , 256 GB RAM) , the theoretical model requires only 46 s to calculate the radiated sound power at a single frequency point, whereas the FEM requires approximately 830 s. The computational time of the theoretical model is merely 1/18 of that required by the FEM, highlighting its high efficiency in analyzing the acoustic radiation of composite periodic ABH plates.

3.2. Sound radiation performance

Fig. 3 compares the radiated sound power of the composite ABH plate and that of a uniform reference plate, both with and without damping layers. The bandgap ranges of the corresponding infinite periodic ABH plate are also indicated: the light gray region denotes the directional flexural wave bandgap and the dark gray region the

Table 1
Geometrical and material parameters of the ABH plate and the damping layers (denoted by subscript d).

Geometry	Material
$a = 100$ mm	$E = 70$ GPa
$H = 7$ mm	$\eta = 0.005$
$h_0 = 0.3$ mm	$\upsilon = 0.3$
$l_\mathrm{ABH} = 63$ mm	$\rho = 2700$ kg/m^3
$m = 3$	$E_\mathrm{d} = 5$ GPa
$h_\mathrm{d} = 0.25$ mm	$\eta_\mathrm{d} = 0.3$
$R_\mathrm{d} = 47.25$ mm	$\upsilon_\mathrm{d} = 0.3$
	$\rho_\mathrm{d} = 950$ kg/m^3

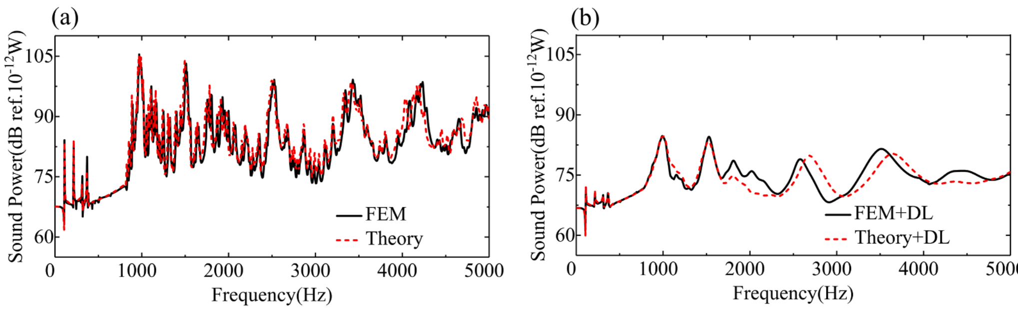

Fig. 2. Comparison between the theoretical and the FEM results for the radiated sound power of the output plate (a) without and (b) with damping layers (DL).

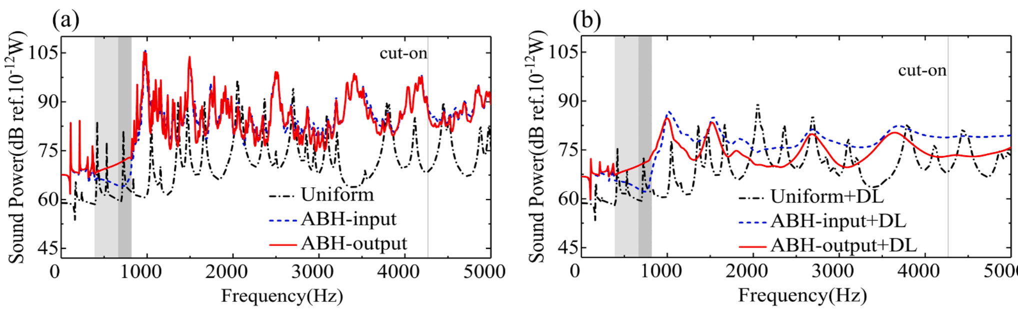

Fig. 3. Radiation sound power comparison between the periodic ABH plate and the counterpart uniform plate (a) without and (b) with damping layers (DL).

complete flexural wave bandgap (this convention is used hereafter). As shown in Fig. 3(a), without damping layers, the ABH plate exhibits a noticeable reduction in the radiated sound power within the bandgap range of 389–819 Hz compared to the uniform plate, particularly at the resonance peaks where reductions up to 16 dB are observed on the output plate. This phenomenon aligns with the observations when the excitation is applied to the uniform region [48]. A distinct feature, however, is the marked difference in the radiated sound power between the input and output plates. Within the bandgap, the input plate radiates systematically less power than the output plate, reaching a maximum difference of 6.5 dB. Outside the bandgap, the sound radiation levels of the input and output plates are rather close to each other but are both notably higher than that of the uniform plate.

With the deployment of the damping layer, as illustrated in Fig. 3(b), the radiated sound power of the uniform plate only marginally decreases. In contrast, for the ABH plate, a pronounced reduction in sound radiation is observed outside the bandgap. More importantly, above 982 Hz, the radiated sound power of the output plate becomes significantly lower than that of the input plate, with an average reduction of 4.2 dB. This asymmetric radiation phenomenon is not observed when the excitation is applied to the uniform region of the ABH structure. Consequently, the output plate achieves comparable and even better sound radiation suppression compared with the uniform plate, with a maximum reduction up to 19 dB. Notably, this effective suppression extends to frequencies far below the cut-on frequency (4268 Hz) of a single ABH unit in this case, as obtained from $f_{\text{cut-on}} = \pi/(2l_{\text{ABH}})^2\sqrt{Eh^2/3\rho(1-\upsilon^2)}$ [47].

Fig. 4 further compares the sound radiation efficiency of the composite ABH plate with that of the uniform plate. Except at very low frequencies and within the bandgap region, the sound radiation efficiency of the ABH plate is lower than that of the uniform plate, regardless of whether damping layers are present, with no significant difference between the input and output plates. Notably, within the bandgap, the sound radiation efficiency of the output plate is comparable to that of the uniform plate, while that of the input plate is significantly reduced. This indicates an effective suppression of the input plate's sound radiation capability within the bandgap, which is consistent with its lower radiated sound power observed in Fig. 3.

It is worth noting that the proposed double-layer ABH configuration achieves these acoustic benefits with significant mass reduction while effectively addressing the inherent stiffness challenge typical of ABH structures. Specifically, the ABH plate considered here attains a 63% mass reduction compared to a uniform plate. More importantly, compared to a traditional single-layer ABH plate with identical ABH parameters, the double-layer design exhibits approximately 2.65 times higher overall flexural stiffness owing to its sandwich-like construction.

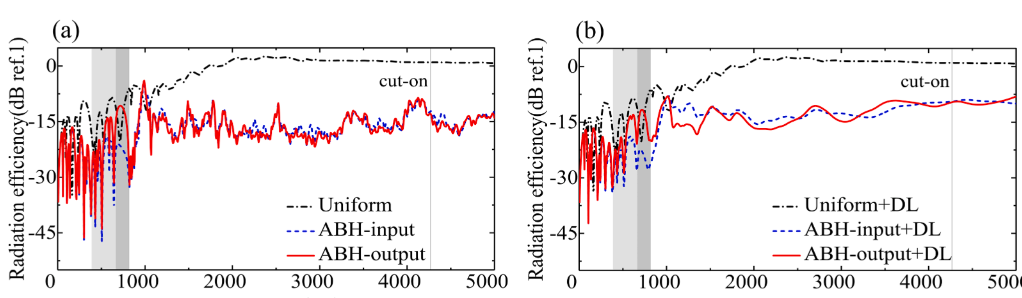

Fig. 4. Radiation efficiency comparison between the periodic ABH plate and the counterpart uniform plate (a) without and (b) with damping layers (DL).

For further details on the enhanced structural stiffness, refer to our previous study on double-layer ABH configurations [57].

To eliminate the influence of mass and stiffness differences, Fig. 5 compares the radiated sound power of the damped ABH plate with a uniform plate with equivalent mass. The results show that the radiated sound power of the ABH plate is significantly lower across nearly the entire frequency range, demonstrating its excellent sound radiation performance over an ultra-wide frequency range.

In summary, compared with a uniform plate of the same mass, the composite periodic ABH plate demonstrates significant advantages in sound radiation mitigation. This structure not only effectively suppresses sound radiation within the bandgap, but also extends the suppression to the non-bandgap frequency range far below the cut-on frequency after adding damping layers, while maintaining a generally lower overall radiation efficiency. Particularly noteworthy is the unique asymmetric sound radiation phenomenon observed under the excitation in the ABH region: within the bandgap, both the sound radiation efficiency and the power of the input plate are lower than those of the output plate; outside the bandgap, the radiated sound power of the output plate becomes significantly lower than that of the input plate with damping layers.

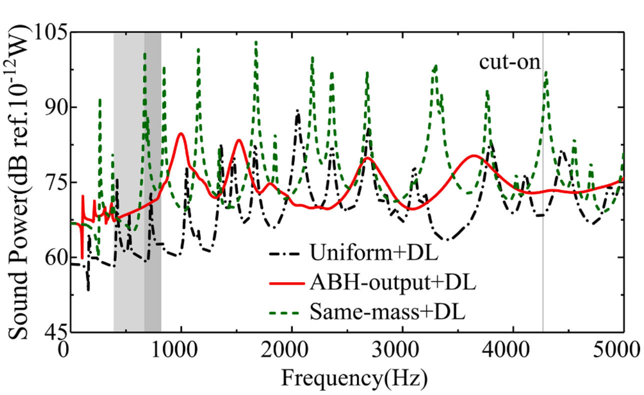

Fig. 5. Sound power comparison between the output plate of the damped periodic ABH structure and a uniform plate with equivalent mass.

3.3. Sound radiation mechanism analyses

To explore the mechanisms underpinning the low sound radiation efficiency and asymmetric sound radiation of the composite periodic ABH plate, wavenumber spectrum and structural intensity analyses are performed. Typical frequencies, both inside and outside the bandgap, are selected and compared with the corresponding uniform plate. Since adding damping layers has no significant effect on the sound radiation efficiency of the ABH plate, the following analysis mainly focuses on the undamped cases.

Outside the bandgap (e.g., 2500 Hz), the wavenumber spectra are compared in Fig. 6. For both the input and output plates of the ABH structure, the vibration energy shifts markedly toward higher wavenumber regions outside the radiation circle. This results in substantially reduced energy in the supersonic components within and near the radiation circle compared to the uniform plate, thereby attenuating far-field sound radiation. This explains the lower sound radiation efficiency of the ABH plate shown in Fig. 4(a), which fundamentally arises from the ABH-induced reduction in flexural wave phase velocity, promoting energy transfer from supersonic to subsonic components [48, 58].

Within the bandgap (e.g., 720 Hz), Fig. 7 reveals that the input plate of the ABH structure exhibits a more pronounced energy shift toward higher wavenumber regions outside the radiation circle compared to the output plate. This distinct difference in wavenumber-domain energy distribution leads to lower sound radiation efficiency observed for the input plate relative to both the output and uniform plate.

To further elucidate the origin of the observed differences in sound radiation efficiency and radiated power between the geometrically identical input and output ABH plates, their vibration response and structural intensity fields are analyzed.

Fig. 8 compares the MQVs of the ABH plate and the uniform plate. Without damping layers as shown in Fig. 8(a), outside the bandgap, the vibration levels of the input and output plates are nearly identical, which both are significantly higher than the uniform plate, attributable to the 63% reduction in mass and 30.8% decrease in overall flexural stiffness. Within the bandgap, the vibration level of the ABH plate decreases significantly, verifying the crucial role of the bandgap in vibration suppression. Notably, the output plate exhibits a lower vibration level than the input plate. With damping layers added (Fig. 8(b)), the vibration of the ABH plate is effectively reduced. Furthermore, as frequency increases, the vibration response of the output plate becomes systematically lower than that of the input plate. Given that the sound radiation efficiencies of the two plates do not differ significantly (see Fig. 4), it indicates that the distinctive difference in radiated sound power primarily originates from the disparity in their vibration levels.

To quantify the vibration level difference, Fig. 9 displays the MQV difference between the input and output plates with and without damping layers. Without damping layers, a significant difference appears mainly within the bandgap, where the output plate shows lower MQV. With damping layers, the difference is markedly amplified above 1500 Hz, exhibiting a systematic separation where the vibration of the output plate is substantially more impaired. This indicates that damping treatment enhances the vibration control capability of the composite periodic ABH structure from a localized bandgap dominant manner to a global broadband character. Interestingly, within the complete bandgap, the vibration difference under damped conditions is slightly smaller than undamped conditions, implying the counteraction between the efficient damping dissipation induced by the ABH effect and the energy distribution regulation arising from the periodic bandgap in the composite double-layer ABH structure.

To better understand the energy regulation mechanism, Fig. 10 and Fig. 11 present the structural intensity and vibration displacement fields of the input and output plates at representative frequencies. Within the bandgap, for the undamped case (Fig. 10(a) and (b)), vibrational energy input at the excitation point on the input plate is confined near the excited unit due to the bandgap effect. Specifically, the input energy is largely concentrated within the ABH region where it is excited. In contrast, for the output plate, vibrational energy enters through the uniform connecting region near the excitation point and does not fully penetrate the ABH region. Consequently, the ABH-induced wave velocity reduction in the input plate shifts its energy distribution toward higher wavenumbers (as shown in Fig. 7(a)), leading to its reduced sound radiation efficiency in Fig. 4(a). The impeded energy transfer from the input to output plate also results in the observed vibration level difference. A similar pattern is observed with damping layers (Fig. 10(c) and (d)). In addition, the displacement of the damped input plate is slightly smaller than undamped one, while that of the output plate remains almost unchanged, resulting in a larger vibration level difference for the case without damping layers.

Outside the bandgap, for the undamped case (Fig. 11(a) and (b)), energy flow distributes across the entire plate and primarily concentrates in the ABH regions, reflecting the typical ABH energy focalization effect. The vibration responses of the two plates remain similar without effective energy dissipation. After coating damping layers (Fig. 11(c) and (d)), the highly concentrated input energy of the input plate is effectively dissipated. Only a small fraction of energy is transmitted through the connecting region to the output plate, where it is again concentrated and efficiently dissipated. This unique double-layer energy flow mechanism results in a much lower vibration response in the output plate compared to the input plate.

To verify the influence of the ABH effect on the vibration level

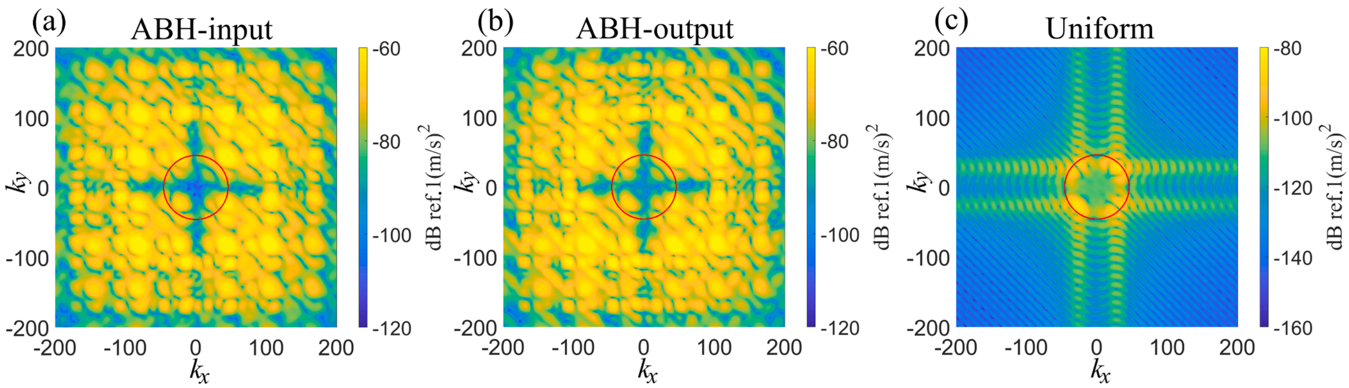

Fig. 6. Wavenumber comparison between the periodic ABH plate and the uniform plate at $f = 2500$ Hz above the bandgap, with red solid line denoting the radiation circle.

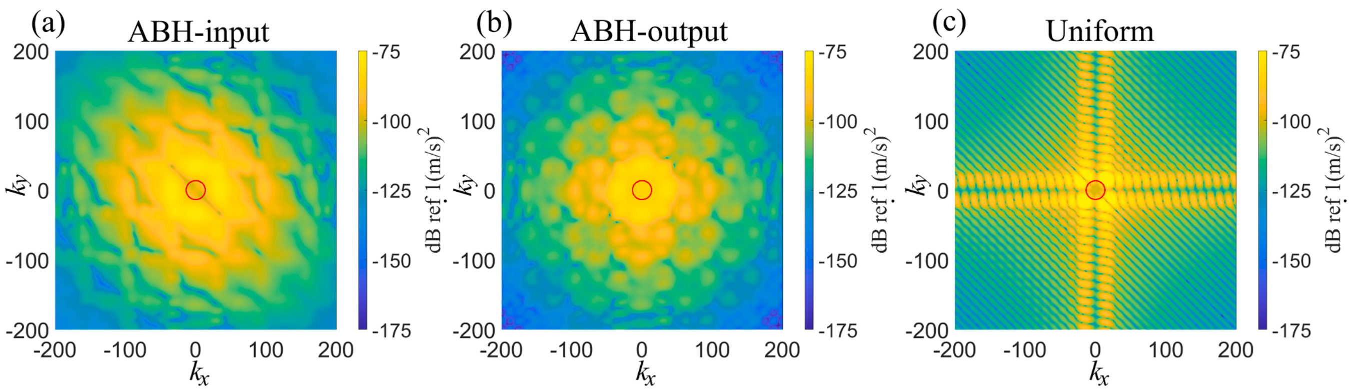

Fig. 7. Wavenumber comparison between the periodic ABH plate and the uniform plate at $f = 720$ Hz within the bandgap, with red solid line denoting the radiation circle.

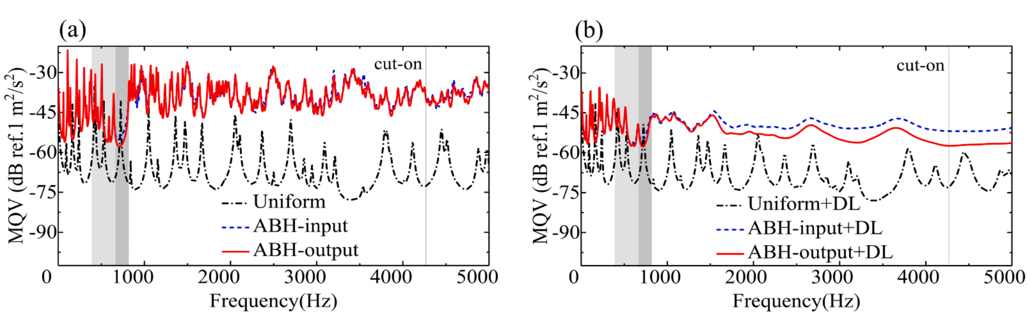

Fig. 8. MQV comparison between the periodic ABH plate and the counterpart uniform plate (a) without and (b) with damping layers (DL).

difference between the two plates, Fig. 12 further compares the MQV difference under different truncation thicknesses h_0. As h_0 decreases, the MQV difference increases significantly. This is because a smaller h_0 strengthens the ABH energy concentration, causing more energy to be concentrated and dissipated during the transmission between the two plates, thereby promoting asymmetric vibration responses. This directly demonstrates the important role of the ABH effect in regulating vibration energy distribution in composite double-layer structures.

4. Experimental validation

To validate the numerically predicted sound radiation characteristics of the composite periodic ABH plate, experiments were performed on a specimen with 4×4 unit cells in an anechoic chamber (cut-off frequency: 80 Hz). The specimen was fabricated via 3D printing, with a mass density of 2593 kg/m^3 , Young's modulus of 70 GPa, Poisson's ratio of 0.3, and damping loss factor of 0.002. The geometric parameters of the structure were: $a = 100$ mm, H= 9.2 mm, $h_0 = 0.6$ mm, $m = 3$ and $l_{ABH} = 63$ mm. A multi-layer 3 M™ F9473PC tape was applied to the surface of the ABH region as the damping layer, with a radius of 45 mm and total thickness of 0.5 mm. To further increase the energy dissipation capacities of the soft damping material, a polycoated Kraft liner was bounded on the outside surface of the damping tape. This liner serves as a constraining layer, creating a constrained layer damping configuration that enhances shear deformation and energy dissipation in the soft viscoelastic damping tape. Similar sandwich damping treatments have been employed in other ABH experimental studies [59,60].

The experimental setup is shown in Fig. 13(a). The tested plate was suspended by two thin strings at the center of a thick wooden baffle of 2400 mm × 2400 mm× 18 mm, with a 1.5 mm gap between the specimen and the baffle. As shown in Fig. 13(b), the excitation system consisted of an electromagnetic shaker (DongHua Testing DH40200) driven

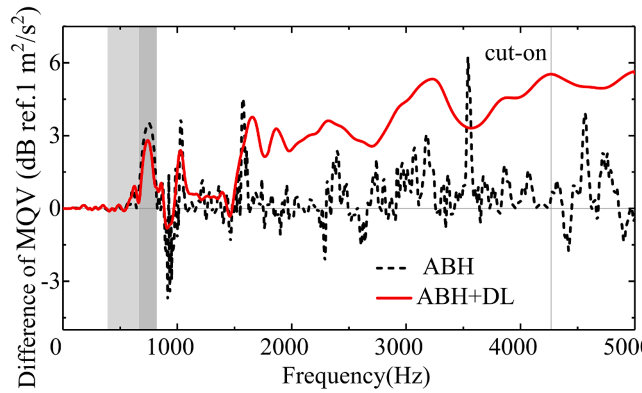

Fig. 9. MQV difference between the input and output plates of the periodic ABH structure without and with damping layers.

by a power amplifier (DongHua Testing DH5872). A swept sine signal generated by a signal generator (DongHua Testing DH1301) served as the excitation source, applied on the panel at (17.5 mm, 17.5 mm). The excitation force was measured with an impedance head (Kistler 8770A5), while the radiated sound pressure was acquired with microphones (Megasig M663 +A802). To minimize background noise, the shaker was enclosed in a thick-walled box filled with sound-absorbing cotton. All data were collected using a data acquisition system (DongHua Testing DH5922D) for subsequent processing and analyses.

The radiated sound power was obtained through sound pressure measurements according to the international standard ISO 3744 [61, 62]. Twenty microphones were located over a hemisphere with a radius $R = 1200$ mm to measure the sound pressure level $L'_{pi(ST)}\,(i = 1,2,\ldots20)$. Due to the limited number of microphones, the sound pressure levels at the 20 measurement positions were measured sequentially by moving three microphones according to the standard's coordinate grid. The radiation sound power was obtained by $L_W = \overline{L_p} + 10\,\mathrm{lg}\,\frac{S}{S_0}$, where $S = 2\pi R^2$ is the area of the hemispherical surface, $S_0 = 1\ \mathrm{m}^2$ is the reference area, and $\overline{L_p}$ is the surface time-averaged sound pressure level obtained from $\overline{L_p} = 10\,\mathrm{lg}\left[\frac{1}{N_M}\sum_{i=1}^{N_M}10^{0.1L'_{pi(ST)}}\right] - K_1$. Here, K_1 is the background noise correction given by $K_1 = -10\,\mathrm{lg}(1-10^{-0.1\Delta L_p})$ with $\Delta L_p = 10\,\mathrm{lg}\left[\frac{1}{N_M}\sum_{i=1}^{N_M}10^{0.1L'_{pi(ST)}}\right] - 10\,\mathrm{lg}\left[\frac{1}{N_M}\sum_{i=1}^{N_M}10^{0.1L'_{pi(B)}}\right]$, $L'_{pi(B)}\,(i = 1,2,\ldots20)$ being the background sound pressure level and $N_M = 20$.

The experimental results are presented in Fig. 14. Without the damping layer (shown in Fig. 14(b)), a broad attenuation band in sound radiation is observed within the predicted bandgap of approximately 650–1100 Hz, where the radiated sound power is significantly reduced. Notably, within this bandgap, the radiated sound power of the input plate is obviously lower than that of the output plate. Outside the bandgap, the radiated sound power curves of the input and output plates show good consistency without obvious differences. The overall trends of the experimental measurements and theoretical predictions are basically consistent in terms of peak positions and amplitude levels, confirming the reliability of the theoretical model. The discrepancies mainly originate from the local machining errors of the ABH plate and

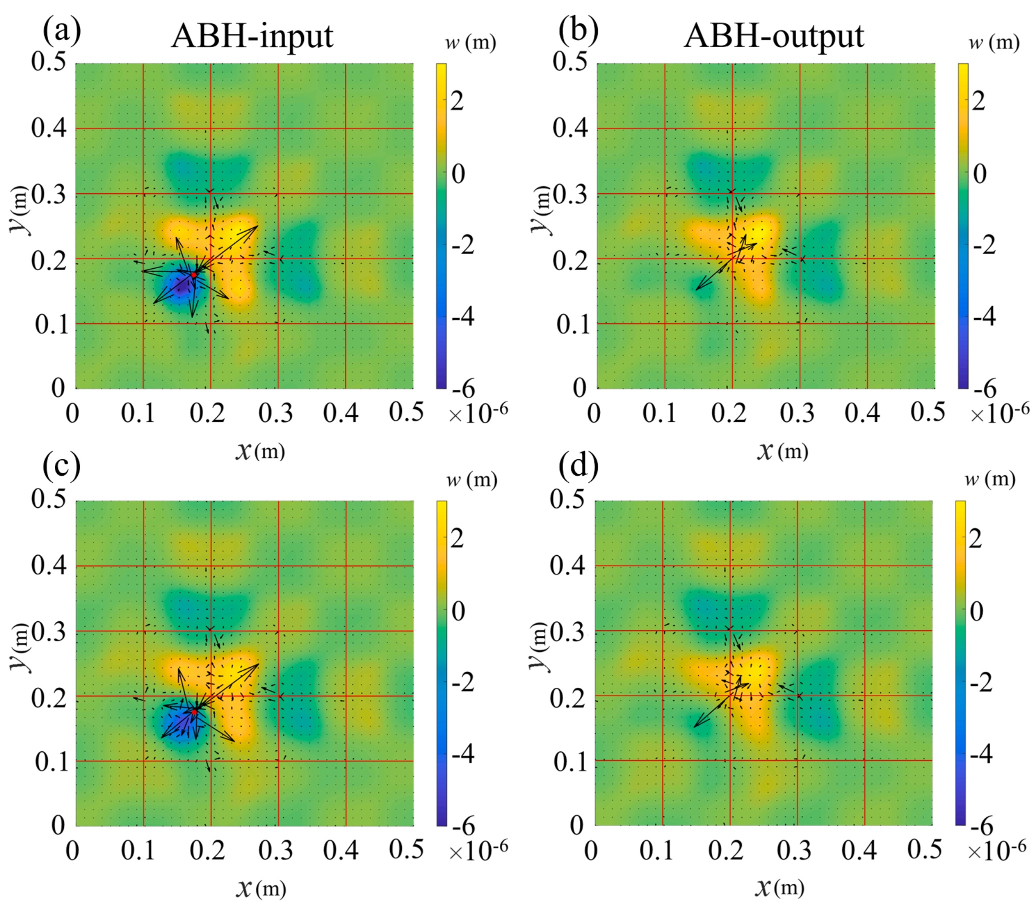

Fig. 10. Structural intensity (vectors) and displacement distribution (colormap) comparison between the input and output plates of the periodic ABH structure at $f = 720$ Hz within the bandgap (a) (b) without and (c) (d) with damping layers. The black arrows, red dots and red lines denote the structural intensity vectors, excitation points and element boundaries, respectively.

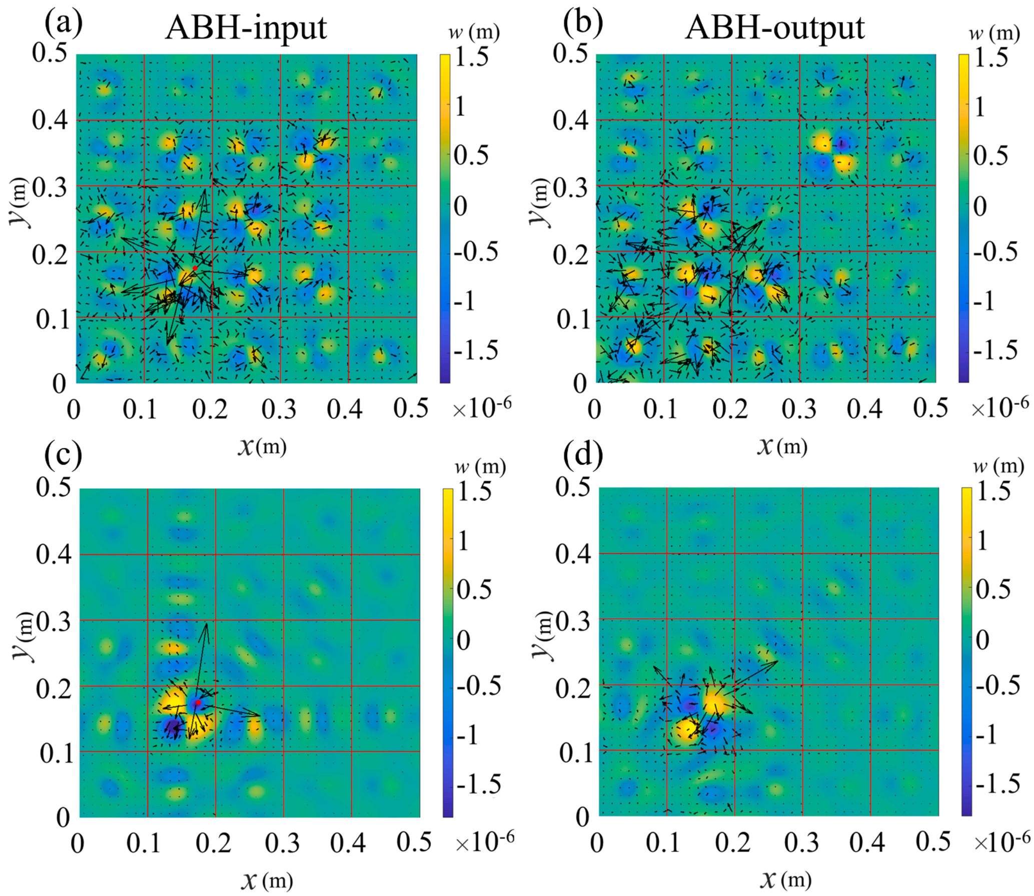

Fig. 11. Structural intensity (vectors) and displacement distribution (colormap) comparison between input and output plates of the periodic ABH structure at $f = 2500$ Hz above the bandgap (a) (b) without and (c) (d) with damping layers. The black arrows, red dots and red lines denote the structural intensity vectors, excitation points and element boundaries, respectively.

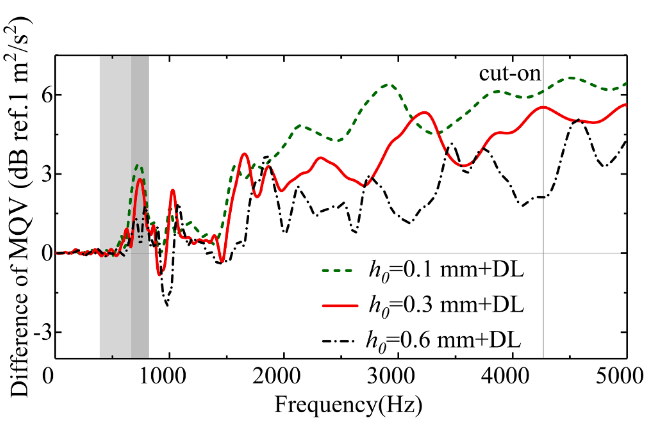

Fig. 12. MQV differences between the input and output plates of the periodic ABH structure with different truncation thicknesses (h_0).

environmental background noise. After adding damping layers (Fig. 14(c)), a comparison with Fig. 14(b) reveals a significant overall reduction in radiated sound power for both the input and output plates. Moreover, the output plate exhibits a more pronounced suppression, systematically radiating less power than the input plate within the 1322–1754 Hz range and above 2360 Hz. This observation aligns with the theoretically predicted phenomenon of asymmetric radiated sound power between the two plates.

5. Conclusions

This study establishes an efficient and accurate semi-analytical theoretical model for the acoustic radiation analysis of composite periodic ABH plates. The model is used to systematically investigate their sound radiation performance and to elucidate the underlying physical mechanisms. The main conclusions are as summarized follows:

(1) The proposed semi-analytical model demonstrates excellent agreement with FEM simulations in predicting both radiated sound power and vibration responses, thereby verifying its accuracy and efficacy. In terms of computational efficiency, the proposed model requires only about 1/18 of the time consumed by a comparable FEM analysis, thereby providing an efficient and reliable tool for acoustic analysis and optimal design of similar complex structures.

(2) Both theoretical and experimental results confirm that the composite double-layer periodic ABH plate entails remarkable broadband sound radiation suppression compared with a uniform plate of equivalent mass. This structure not only effectively reduces sound radiation within its bandgap, but also extends the suppression effect to a wide non-bandgap frequency range far below the cut-on frequency of the ABH unit when damping layers are applied, while maintaining a lower overall sound radiation efficiency. A salient feature arising from the double-layer ABH design is the asymmetric sound radiation from the input and output plates with an excitation directly applied to the ABH region. Within the bandgap, this phenomenon contributes to lower sound radiation from the input plate; outside the bandgap, it leads to the drastic sound radiation suppression from the output plate.

(3) The structure's excellent sound radiation performance and unique asymmetric sound radiation phenomenon is attributed to two

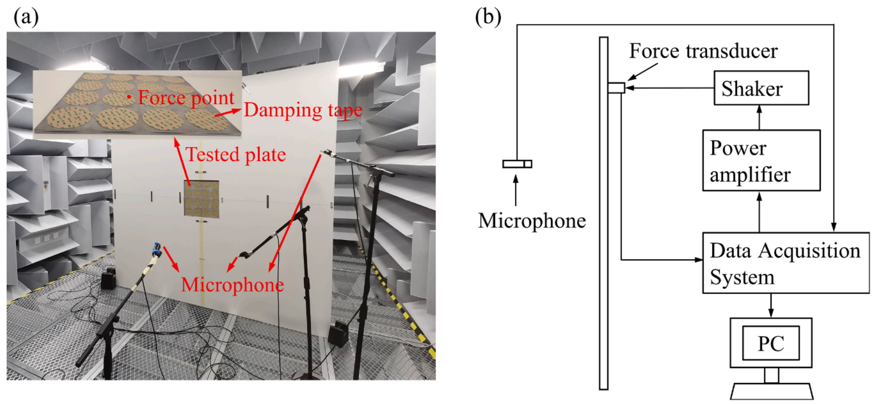

Fig. 13. Experimental setup for radiation sound power test: (a) schematic of the test sample; (b) measurement system.

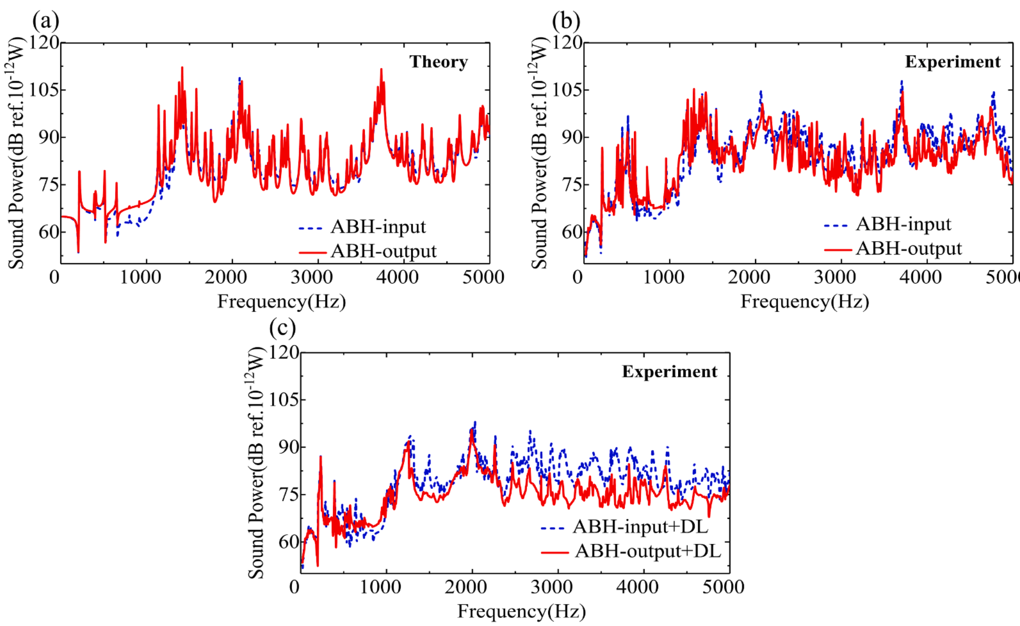

Fig. 14. Comparisons of radiated sound power between the input and output plates of the periodic ABH structure: (a) theoretical and (b) experimental results without damping layers; (c) experimental results with damping layers.

synergistic mechanisms. First, the ABH effect plays a fundamental regulatory role in reducing the flexural wave velocity, transferring vibration energy from supersonic to subsonic component, thereby systematically reducing the sound radiation efficiency. Concurrently, its energy concentration effect allows for highly efficient energy dissipation through the damping layers. Second, synergetic effects among periodic bandgap, the double-layer configuration and damping dissipation are observed. Within the bandgap, the periodic layout localizes energy near the excitation point, which, combined with the ABH effect, confines and concentrates energy differently in each plate, namely primarily within the ABH region for the input plate and the connecting uniform region for the output plate. This energy distribution difference leads to the asymmetric sound radiation efficiency between the two plates. Outside the bandgap, the double-layer design works in concert with damping treatment to achieve a sequential energy concentration-dissipation process. Input energy is first concentrated and dissipated in the ABH region of the input plate, and the residual energy transmitted to the output plate undergoes further concentration and dissipation. This process enables vibration reduction of the output plate and the consequent radiated sound power.

In summary, the semi-analytical model developed in this study, while building upon the established GEM, demonstrates its effective extension to double-layer periodic ABH plates and provides an efficient tool for analyzing such complex layered metastructures. The study reveals the synergistic mechanisms involving wave velocity regulation via the ABH effect, energy localization via periodic bandgap, and energy flow and dissipation in a layered design. The proposed composite double-layer periodic ABH plate, with its lightweight feature, higher structural stiffness than conventional single-layer ABH plates, and broadband sound suppression, shows promise for applications in aerospace structures (e.g., satellite panels, aircraft cabins), high-speed transportation vehicles, and marine vessels where both weight reduction and vibration/noise control are critical. The observed asymmetric vibration and sound radiation phenomena also offer new insights for developing smart structures with direction-dependent acoustic properties.

CRediT authorship contribution statement

Yuguang Chen: Writing – original draft, Visualization, Investigation, Formal analysis, Data curation. **Fatao Ye:** Validation, Data curation. **Debin Li:** Software, Data curation. **Jie Deng:** Writing – review & editing, Investigation. **Li Cheng:** Writing – review & editing, Methodology. **Liling Tang:** Writing – review & editing, Supervision, Resources, Methodology, Conceptualization.

Declaration of Competing Interest

The authors declare that they have no known competing financial interests or personal relationships that could have appeared to influence the work reported in this paper.

Acknowledgments

This work was supported by the Guangdong Basic and Applied Basic Research Foundation (No. 2024A1515011511).

Appendix A. . Derivation of Equation (20)

The internal forces and moments of structure can be described as:

$$M_x = -D\left(\frac{\partial^2 w}{\partial x^2} + \upsilon \frac{\partial^2 w}{\partial y^2}\right) \tag{A.21}$$

$$M_y = -D\left(\frac{\partial^2 w}{\partial y^2} + \upsilon \frac{\partial^2 w}{\partial x^2}\right) \tag{A.22}$$

$$M_{xy} = M_{yx} = -D(1-\upsilon)\frac{\partial^2 w}{\partial x \partial y} \tag{A.23}$$

$$Q_x = -D\frac{\partial}{\partial x}\left(\nabla^2 w\right) \tag{A.24}$$

$$Q_y = -D\frac{\partial}{\partial y}\left(\nabla^2 w\right) \tag{A.25}$$

$$N_x = D_E\left(\frac{\partial u}{\partial x} + \upsilon \frac{\partial v}{\partial y}\right) \tag{A.26}$$

$$N_y = D_E\left(\upsilon\frac{\partial u}{\partial x} + \frac{\partial v}{\partial y}\right) \tag{A.27}$$

$$N_{xy} = N_{yx} = D_E\left(\frac{1-\upsilon}{2}\right)\left(\frac{\partial u}{\partial x} + \upsilon \frac{\partial v}{\partial y}\right) \tag{A.28}$$

Appendix B. Effect of damping layer coverage ratio on sound radiation performance

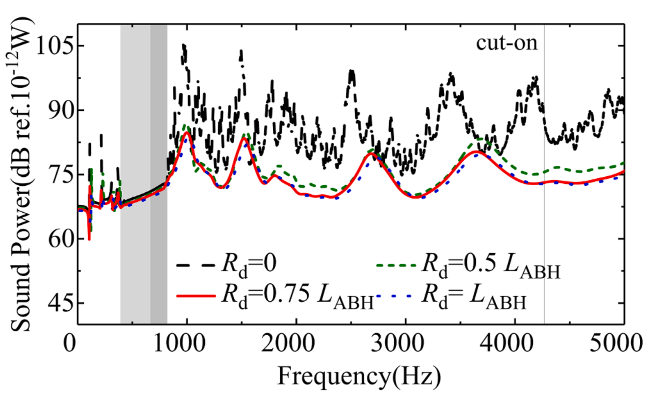

Fig. B1. Comparison of the radiated sound power of the periodic ABH structure under different damping coverage ratios.

.

Figure B.1 compares the radiated sound power of the periodic ABH plate under three different damping coverage ratios, i.e. 50%, 75% (the value adopted in the main manuscript), and 100% (full coverage of the ABH region). The undamped case $R_d = 0$ is also included as a baseline. Compared with the undamped structure, all three coverage ratios significantly reduce the radiated sound power. The 75% coverage yields a reduction that is almost indistinguishable from the full 100% coverage across most of the frequency range. The 50% coverage, while slightly less effective than 75%, still provides a substantial suppression compared to the undamped case. Based on these results, the 75% coverage was selected in the main manuscript as a balanced choice that achieves near-optimal performance while minimizing the use of damping material. The observation that the structure remains effective even at 50% coverage further confirms the robustness of the proposed design.

Data availability

Data will be made available on request.

References

[1] V.V. Krylov, F.J.B.S. Tilman, Acoustic 'black holes' for flexural waves as effective vibration dampers, J. Sound. Vib. 274 (2004) 605–619.
[2] A. Pelat, F. Gautier, S.C. Conlon, F. Semperlotti, The acoustic black hole: a review of theory and applications, J. Sound. Vib. 476 (2020) 115316.
[3] Y. Zhang, W. Che, H. Qin, X. Rui, L. Cheng, G. Wang, F. Yang, Deep-subwavelength ultra-low and ultra-broadband acoustic-black-hole metamaterials, Nat. Commun. 16 (2025) 11276.
[4] V.B. Georgiev, J. Cuenca, F. Gautier, L. Simon, V.V. Krylov, Damping of structural vibrations in beams and elliptical plates using the acoustic black hole effect, J. Sound. Vib. 330 (2011) 2497–2508.
[5] L. Tang, L. Cheng, H. Ji, J. Qiu, Characterization of acoustic black hole effect using a one-dimensional fully-coupled and wavelet-decomposed semi-analytical model, J. Sound. Vib. 374 (2016) 172–184.
[6] C. Yang, T. Ye, M. Qiu, Z. Zhai, P. Hu, A semi-analytical framework for comprehensive vibration analysis of segment-coupled plates with embedded acoustic black holes, Thin Wall. Struct. 184 (2023) 110517.
[7] S. Park, M. Kim, W. Jeon, Experimental validation of vibration damping using an Archimedean spiral acoustic black hole, J. Sound. Vib. 459 (2019) 114838.
[8] P.A. Feurtado, S.C. Conlon, An Experimental Investigation of Acoustic Black Hole Dynamics at Low, Mid, and High Frequencies, J. Acoust. Soc. Am. 138 (2016) 061002.
[9] H. Li, M. Sécail-Géraud, A. Pelat, F. Gautier, C. Touzé, Experimental evidence of energy transfer and vibration mitigation in a vibro-impact acoustic black hole, Appl. Acoust. 182 (2021) 108168.
[10] F. Liu, P. Shi, Y. Shen, Y. Xu, Z. Yang, Advances in suppression of structural vibration and sound radiation by flexural wave manipulation, Thin Wall. Struct. 200 (2024) 111936.
[11] S.C. Conlon, J.B. Fahnline, F. Semperlotti, Numerical analysis of the vibroacoustic properties of plates with embedded grids of acoustic black holes, J. Acoust. Soc. Am. 137 (2015) 447–457.
[12] X. Li, Q. Ding, Sound radiation of a beam with a wedge-shaped edge embedding acoustic black hole feature, J. Sound. Vib. 439 (2019) 287–299.
[13] L. Ma, S. Zhang, L. Cheng, A 2D Daubechies wavelet model on the vibration of rectangular plates containing strip indentations with a parabolic thickness profile, J. Sound. Vib. 429 (2018) 130–146.
[14] H. Ji, X. Wang, J. Qiu, L. Cheng, Y. Wu, C. Zhang, Noise reduction inside a cavity coupled to a flexible plate with embedded 2-D acoustic black holes, J. Sound. Vib. 455 (2019) 324–338.
[15] J. Liu, Y. Zhang, H. Jia, X. Rui, X. Yan, G. Wang, Y. Liu, Noise reduction of add-on acoustic black holes with different topologies based on combined Reduced Multibody System Transfer Matrix Method and Elementary Radiators Method, Thin Wall. Struct. 214 (2025) 113366.
[16] H. Ye, C. Wang, C. Tao, H. Ji, J. Qiu, Sound radiation suppression in a plate-cavity coupling system under acoustic excitation using ABH-DVA, Thin Wall. Struct. 207 (2025) 112741.
[17] L. Tang, L. Cheng, Enhanced Acoustic Black Hole effect in beams with a modified thickness profile and extended platform, J. Sound. Vib. 391 (2017) 116–126.
[18] L. Tang, L. Cheng, Loss of acoustic black hole effect in a structure of finite size, Appl. Phys. Lett. 109 (2016) 014102.
[19] F. Semperlotti, H. Zhu, Phononic thin plates with embedded acoustic black holes, Phys. Rev. B 91 (2015) 104304.
[20] N. Gao, Z. Wei, R. Zhang, H. Hou, Low-frequency elastic wave attenuation in a composite acoustic black hole beam, Appl. Acoust. 154 (2019) 68–76.
[21] P. Halevi, L. Dobrzynski, B. Djafari-Rouhani, M.S. Kushwaha, Acoustic band structure of periodic elastic composites, Phys. Rev. Lett. 71 (1993) 2022–2025.
[22] Z. Liu, X. Zhang, Y. Mao, Y.Y. Zhu, Z. Yang, C.T. Chan, P. Sheng, Locally Resonant Sonic Materials, Science 289 (2000) 1734–1736.
[23] Y. Bu, Y. Tang, J. Wu, T. Yang, Q. Ding, Y. Li, Novel vibration suppression of spinning periodically acoustic black hole pipes based on the band-gap mechanism, Thin Wall. Struct. 212 (2025) 113198.
[24] X. Lyu, H. Sheng, M. He, Q. Ding, L. Tang, T. Yang, Satellite Vibration Isolation Using Periodic Acoustic Black Hole Structures with Ultrawide Bandgap, J. Acoust. Soc. Am. 145 (2023) 014501.
[25] J. Deng, N. Gao, X. Chen, B. Han, H. Ji, Evanescent waves in a metabeam attached with lossy acoustic black hole pillars, Mech. Syst. Signal. Pr. 191 (2023) 110182.
[26] L. Zhao, Low-frequency vibration reduction using a sandwich plate with periodically embedded acoustic black holes, J. Sound. Vib. 441 (2019) 165–171.
[27] N. Gao, B. Wang, K. Lu, H. Hou, Complex band structure and evanescent Bloch wave propagation of periodic nested acoustic black hole phononic structure, Appl. Acoust. 177 (2021) 107906.
[28] B. Ye, P. Wang, Z. Zhao, H. Jia, Z. Zhang, S. Duan, C. Liu, H. Lei, Inhomogeneous acoustic black hole lattice design for superior vibration suppression, Int. J. Mech. Sci. 306 (2025) 110845.
[29] X. Lyu, H. Li, Z. Ma, Q. Ding, T. Yang, L. Chen, K.K. Żur, Numerical and experimental evidence of topological interface state in a periodic acoustic black hole, J. Sound. Vib. 514 (2021) 116432.
[30] Y. Bao, Z. Yao, Y. Zhang, X. Hu, X. Liu, Y. Shan, T. He, Ultra-broadband gaps of a triple-gradient phononic acoustic black hole beam, Int. J. Mech. Sci. 265 (2024) 108888.
[31] J. Deng, L. Zheng, Noise reduction via three types of acoustic black holes, Mech. Syst. Signal. Pr. 165 (2022) 108323.
[32] J. Deng, N. Gao, X. Chen, Ultrawide attenuation bands in gradient metabeams with acoustic black hole pillars, Thin Wall. Struct. 184 (2023) 110459.
[33] Z. Yao, Y. Bao, X. Liu, Y. Shan, T. He, Vibration and noise reduction characteristics of double-layer stiffened plates embedded with acoustic black holes, Appl. Acoust. 237 (2025) 110767.
[34] W. Gao, Z. Qin, F. Chu, Broadband vibration suppression of rainbow metamaterials with acoustic black hole, Int. J. Mech. Sci. 228 (2022) 107485.
[35] S. Park, W. Jeon, Concave-shaped acoustic black holes with asymmetric arrangement for suppression and amplification of structural vibration, J. Sound. Vib. 600 (2025) 118885.
[36] Z. Wan, X. Zhu, T. Li, Y. Han, W. Guo, A combined periodic acoustic black hole beams with wide vibration attenuation bands, Thin Wall. Struct. 193 (2023) 111221.
[37] H. Ji, B. Han, L. Cheng, D.J. Inman, J. Qiu, Frequency attenuation band with low vibration transmission in a finite-size plate strip embedded with 2D acoustic black holes, Mech. Syst. Signal. Pr. 163 (2022) 108149.
[38] S. Nair, M. Jokar, F. Semperlotti, Nonlocal acoustic black hole metastructures: achieving broadband and low frequency passive vibration attenuation, Mech. Syst. Signal. Pr. 169 (2022) 108716.
[39] L. Tang, S. An, Y. Chen, D. Li, L. Cheng, Broadband unidirectional vibration transmissibility governed by an eigenfrequency-transmissibility correlation, Int. J. Mech. Sci. 307 (2025) 110927.
[40] T. Zhou, L. Cheng, Planar Swirl-shaped Acoustic Black Hole Absorbers for Multi-directional Vibration Suppression, J. Sound. Vib. 516 (2022) 116500.
[41] N. Gao, Z. Zhang, Y. Li, G. Pan, Experimental verification of ultra-broadband vibration reduction of underwater vehicle pressure-resisting shells using acoustic black holes, Thin Wall. Struct. 211 (2025) 113118.
[42] H. Ji, N. Wang, C. Zhang, X. Wang, L. Cheng, J. Qiu, A vibration absorber based on two-dimensional acoustic black holes, J. Sound. Vib. 500 (2021) 116024.
[43] Y. Li, Q. Huang, S. Yao, C. Shi, Wave propagation and vibration attenuation in spiral ABH metamaterial beams, Int. J. Mech. Sci. 269 (2024) 108976.
[44] D. Martins, M. Karimi, L. Maxit, Semi-analytical formulation to predict the vibroacoustic response of a fluid-loaded plate with ABH stiffeners, Thin Wall. Struct. 205 (2024) 112539.
[45] L. Tang, L. Cheng, Ultrawide band gaps in beams with double-leaf acoustic black hole indentations, J. Acoust. Soc. Am. 142 (2017) 2802–2807.
[46] L. Tang, L. Cheng, Periodic plates with tunneled Acoustic-Black-Holes for directional band gap generation, Mech. Syst. Signal. Pr. 133 (2019) 106257.
[47] L. Tang, L. Cheng, Impaired sound radiation in plates with periodic tunneled Acoustic Black Holes, Mech. Syst. Signal. Pr. 135 (2020) 106410.
[48] L. Tang, N. Gao, J. Xu, K. Chen, L. Cheng, A light-weight periodic plate with embedded acoustic black holes and bandgaps for broadband sound radiation reduction, J. Acoust. Soc. Am. 150 (2021) 3532–3543.
[49] L. Tang, L. Cheng, K. Chen, Complete sub-wavelength flexural wave band gaps in plates with periodic acoustic black holes, J. Sound. Vib. 502 (2021) 116102.
[50] J. Deng, L. Zheng, O. Guasch, H. Wu, P. Zeng, Y. Zuo, Gaussian expansion for the vibration analysis of plates with multiple acoustic black holes indentations, Mech. Syst. Signal. Pr. 131 (2019) 317–334.
[51] J. Deng, N. Gao, L. Tang, H. Hou, K. Chen, L. Zheng, Vibroacoustic mitigation for a cylindrical shell coupling with an acoustic black hole plate using Gaussian expansion component mode synthesis, Compos. Struct. 298 (2022) 116002.
[52] P.A. Feurtado, S.C. Conlon, Wavenumber transform analysis for acoustic black hole design, J. Acoust. Soc. Am. 140 (2016) 718–727.
[53] M. Su, J. Du, Y. Liu, Z. Dai, X. Liu, Vibration and power flow analysis of a uniform beam coupled with an ABH beam with arbitrary angles, Mech. Syst. Signal. Pr. 234 (2025) 112810.
[54] Y. Wang, J. Du, Y. Liu, Dynamic modeling of vibration behavior and power flow of a plate structure embedded with an ABH indentation, Appl. Acoust. 215 (2024) 109724.
[55] D. Jiang, Y. Zhao, R. Guo, M. Chen, Analysis of dynamic modeling and power flow of ABH laminated composite thin beam with elastic boundaries, Thin Wall. Struct. 205 (2024) 112485.
[56] J. Du, Y. Wang, Y. Liu, Vibration behavior and power transmission of coupled plate structures with embedded acoustic black holes joined at an arbitrary angle, Thin Wall. Struct. 197 (2024) 111565.
[57] T. Zhou, L. Tang, H. Ji, J. Qiu, L. Cheng, Dynamic and Static Properties of Double-Layered Compound Acoustic Black Hole Structures, Int. J. Appl. Mech. 09 (2017) 1750074.
[58] L. Ma, L. Cheng, Sound radiation and transonic boundaries of a plate with an acoustic black hole, J. Acoust. Soc. Am. 145 (2019) 164–172.
[59] T. Zhou, L. Cheng, A resonant beam damper tailored with Acoustic Black Hole features for broadband vibration reduction, J. Sound. Vib. 430 (2018) 174–184.
[60] O. Unruh, C. Blech, H.P. Monner, Numerical and Experimental Study of Sound Power Reduction Performance of Acoustic Black Holes in Rectangular Plates, SAE Int. J. Passeng. Cars Mech. Syst. 8 (2015) 956–963.
[61] F. Liu, Y. Xu, P. Peng, F. Wang, J. Zhou, Z. Yang, A meta-plate with radial rainbow reflection effect for broadband suppression of vibration and sound radiation, J. Sound. Vib. 585 (2024) 118428.
[62] ISO 3744–2009, Acoustic-determination of sound power levels of noise sources using sound pressure-engineering method in an essentially free field over a reflecting plane, Brussels: Int. Org. Standardizat. (2009).